RESEARCH ARTICLE

Practical concerns of implementing a finite-time Lyapunov exponent analysis with under-resolved data

Matthew P. Rockwood[1,2] · Thomas Loiselle[1] · Melissa A. Green[1]

Abstract

Using Lagrangian techniques to find transport barriers in complex, aperiodic flows necessitates a careful consideration of the available dimensional support (3D versus 2D) and temporal resolution of the data to be analyzed, a particular challenge in experimental data acquisition. To illustrate and diagnose the detrimental effects that can manifest in the computed Lagrangian flow maps and Cauchy–Green strain tensor that are calculated as part of most Lagrangian coherent structure analyses, planar finite-time Lyapunov exponent (FTLE) fields are computed from analytically defined, experimentally collected, and numerically simulated velocity fields. The FTLE fields calculated using three-component, three-dimensional velocity information (3D FTLE) are compared with calculations using two-dimensional data considering only the in-plane velocities (2D FTLE), data that are typically gathered during fluid dynamics experiments. In some regions, where the vortex rotation axis is perpendicular to the plane of interest, the 2D FTLE may perform well. However, in regions where the vortex rotation axis has a non-zero component parallel to the plane of interest, whole structures can fail to be captured by the 2D FTLE. A quantitative analysis of the error in the 2D FTLE field as it relates to instantaneous vorticity deviation core angle is conducted using Hill's spherical vortex and the wake of a bioinspired pitching panel. The effect of decreasing temporal resolution is studied using simulated 3D experiments of a fully turbulent channel flow, where the time resolution of the velocity data is artificially degraded. The resultant 3D FTLE fields progressively worsen with degrading velocity field temporal resolution by the visible elongation of coherent structures in the streamwise direction, indicative of the poorly resolved intermediate velocity fields. This effect can be mitigated with a simple method that invokes Taylor's frozen eddy hypothesis. Both dimensional support and temporal resolution problems in experimental velocity fields can cause major errors in the resulting FTLE fields. With fundamental understanding about the flow field of interest, such as local vortex orientation or relevant length and time scales, some of the pitfalls may be avoided.
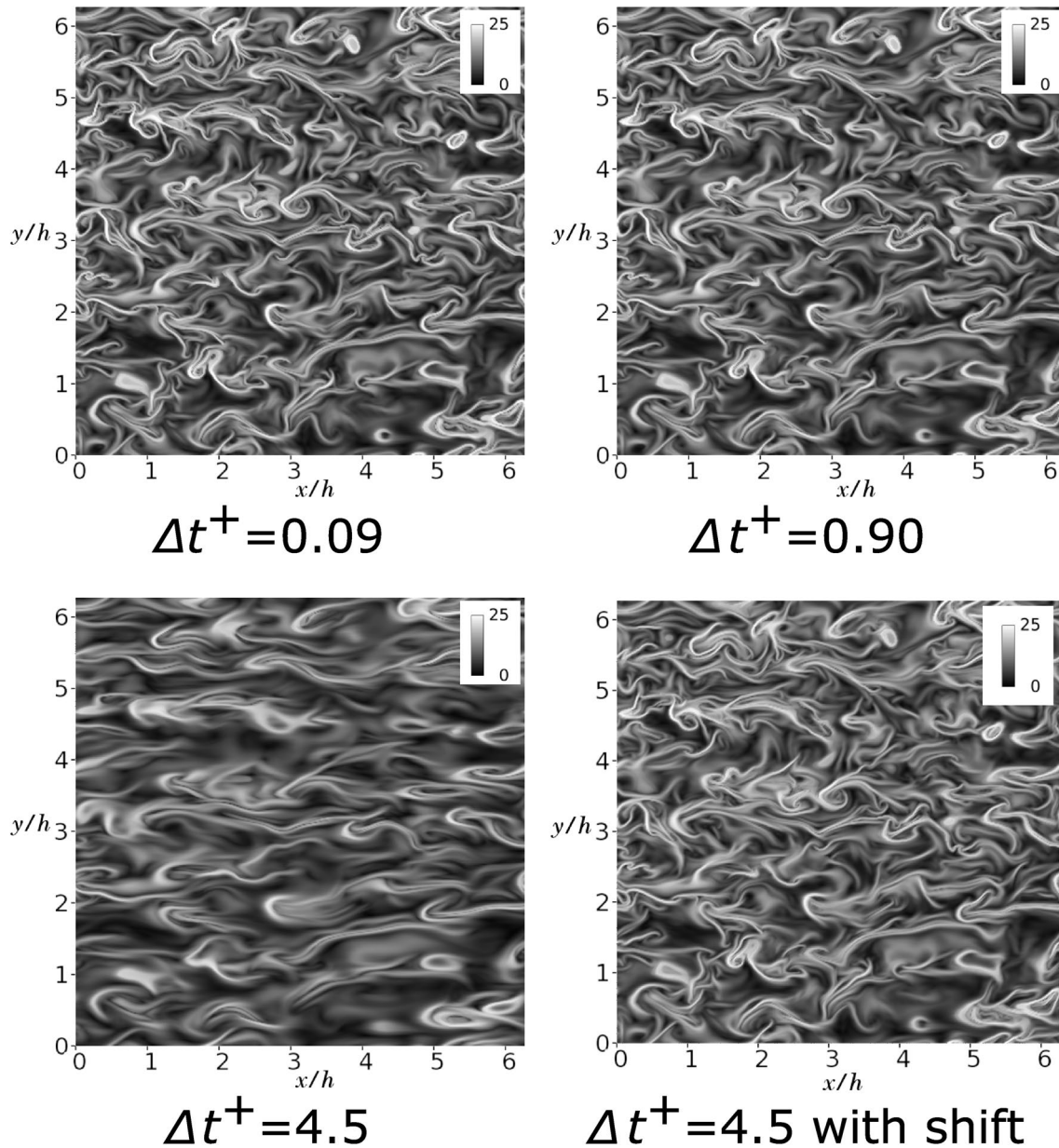
✉ Matthew P. Rockwood
  mprockwo@syr.edu

1 Mechanical and Aerospace Engineering Department,
   Syracuse University, Syracuse, NY 13244, USA

2 Present Address: AS&M, WPAFB, Dayton, OH 45433, USA

Graphical abstract

$$\Delta t^+ = 0.09$$

$$\Delta t^+ = 0.90$$

$$\Delta t^+ = 4.5$$

$$\Delta t^+ = 4.5 \text{ with shift}$$

1 Introduction and motivation

There are numerous criteria that seek to define coherent structures, or vortices, from collected velocity field data using techniques that detect the presence of locally rotating flow, low pressure, or hyperbolic stretching between regions of qualitatively distinct flow. Each of these methods works best in certain situations, but most can provide information in any scenario as long as their relative strengths and limitations are considered. Many commonly used vortex identification analyses, including vorticity or scalar fields such as the Q (Hunt et al. 1988) or Δ (Chong et al. 1990) criteria, are Eulerian. They are computed using the instantaneous velocity field and its derivatives. For that reason, Eulerian criteria can be simple and quick to compute, but share a few disadvantages.

On the other hand, Lagrangian methods define a scalar field at a given time by using the information along

integrated particle trajectories (Haller 2015). In this paper, the finite-time Lyapunov exponent (FTLE) is used as the example Lagrangian quantity as it, like many Lagrangian methods, requires the evaluation of the Cauchy–Green strain tensor, which is constructed from the flow map in the domain of interest. This requires adequate dimensional support and temporal resolution to ensure accurate particle trajectories (Allshouse and Peacock 2015). FTLE ridges are often considered hyperbolic Lagrangian coherent structures (LCS), but that is not the case in general (Haller 2011). Regardless, most techniques used to calculate LCS also rely on the accurate calculation of the Cauchy–Green strain tensor, and, therefore, are subject to the same inaccuracies caused by lack of dimensional support or temporal resolution that may plague FTLE. FTLE is one of the most basic representations of the Cauchy–Green strain tensor among the techniques used to determine LCS, and many techniques used to locate hyperbolic LCS rely on the FTLE fields as the basis for further refinement.

Even on its own, FTLE has proven to be a powerful tool for the purposes of identifying and tracking coherent structures in complex vortex-dominated fluid flows. This method has been used for both periodic (Green et al. 2011; Bourgeois et al. 2012; Kourentis and Konstantinidis 2011; Miron and Vétel 2015; Rockwood et al. 2016; Bose and Sarkar 2018) and aperiodic (Beron-Vera et al. 2008; Blazevski and Haller 2014; O'Farrell and Dabiri 2014; Mulleners and Raffel 2011; du Toit and Marsden 2010) flow fields, and can be implemented using velocity field data from analytical solutions, numerical simulations, and experiments. While methods to find the FTLE field from experimental data are both possible and promising using existing techniques, there is still considerable work to be done to address how the accuracy of Lagrangian scalar fields can be established and when FTLE should be considered less reliable than the instantaneously computed Eulerian criteria. For many complex 3D flows, three-component velocity fields covering a sufficiently large, 3D portion of the fluid domain over a sufficient period of time are achievable experimentally only in special circumstances. It is imperative to develop guidelines and metrics to determine when FTLE analyses can be considered accurate and reliable to most appropriately take advantage of the additional information they can provide on flow physics and dynamics.

The effect of spatial resolution, noise, and smoothing on LCS found as FTLE ridges has previously been investigated by Olcay et al. (2010), who found that poor spatial resolution had a significant impact on the location of the LCS. Several studies have been conducted to investigate how spatial and temporal resolution affects LCS in ocean flows (Beron-Vera 2010; Keating et al. 2011; Hernández-Carrasco et al. 2011; Poje et al. 2010), and found that flows with unresolved small-scale energetic motion can have large errors in the FTLE field, and therefore should be used with caution. Keating et al. (2011) determined that a temporal resolution to spatial resolution ratio below about 1/16 days/km was required to avoid overshoot of small-scale structures in trajectory calculations using ocean models. BozorgMagham and Ross (2015) studied how FTLE results change when small-scale structures are not resolved in atmospheric flows.

Multiple techniques have been introduced that implement a variety of theories to ensure the accuracy of computed LCS. The variational theory method proposed by Haller (2011) found an exact relationship between the LCS and the invariants of the Cauchy–Green strain tensor that allowed for LCS to be defined as the locally strongest attracting or repelling material surfaces. In order to allow the usage of data with low spatial resolution, an approach that used sparse trajectory information presented a cluster-based approach to determine regions of the flow with coherent groups of particles that highlight the dynamically different regions found by FTLE (Froyland and Padberg-Gehle 2015). Tang and Walker (2012) related diffusion statistics to portions of the flow demarcated by LCS, and found good agreement.

There are several techniques that have been proposed that attempt to move away from using the Cauchy–Green strain tensor directly, the majority of which still rely on accurate particle trajectory integration (Balasuriya et al. 2018). One such method uses distinguished trajectories that can reveal both hyperbolic and non-hyperbolic flow regions in time-dependent flows (Rempel et al. 2013). These trajectories are used to find both the stable and unstable manifolds in the same calculation. The function "M" defined by these trajectories is less sensitive to integration time than the standard FTLE calculation and does not use the Cauchy–Green strain tensor, but still relies on accurate tracking of particle trajectories. A study by Banisch and Koltai (2017) determined a method to obtain Lagrangian sets of coherent fluid without using the Cauchy–Green strain tensor, but also relied on accurate tracking of particle trajectories. The finite-size Lyapunov exponent (FSLE) has also been used to extract LCS, but to extract true LCS, the FSLE must meet a stringent set of requirements that increase the difficulty of the calculation (Karrasch and Haller 2013). The calculation of the FSLE field also relies on accurate integration of particle trajectories, and therefore on adequate spatial and temporal resolution (Hernández-Carrasco et al. 2011; Poje et al. 2010). A method proposed by Leung (2011, 2013) and You and Leung (2018) relies on partial differential equations and Eulerian data to predict the FTLE field instead of using particle trajectories and the Cauchy–Green strain tensor. While this method may eliminate the need for accurate particle trajectory information, it has yet to be implemented using experimental data. A method proposed by Froyland et al. (2010) used probabilistic methods to study the evolution of

probability densities to find the regions that remain coherent and relatively non-dispersive.

Any analysis that tracks trajectory behavior through multi-dimensional space and time is subject to possible degradation when short time-scale dynamics or dynamics out of the known dimension are not captured in the acquired data sets. Sulman et al. (2013) investigated FTLE fields calculated with varying magnitudes of out-of-plane shear and velocity magnitude in two steady analytical test cases. Large values of out-of-plane shear of the in-plane velocities were determined to be a significant contributor to errors in 2D FTLE fields that neglected the out-of-plane velocity component. The current study extends this line of thinking into unsteady experimental results and studies the difference between 2D and 3D FTLE as the orientation of nearby coherent structures varies.

In this paper, two main limitations of a Lagrangian analysis are discussed: dimensional support and temporal resolution. Lagrangian methods that depend on tracking fluid trajectories in 3D flow fields are at a disadvantage if the available velocity data only exist in a 2D plane within the flow domain, common in particle image velocimetry (PIV). This is shown by implementing FTLE analyses on the analytical Hill's spherical vortex in Sect. 2.1 and the experimental wake behind a pitching panel in Sect. 2.2. Depending on the organization and alignment of the coherent structures in the flow field, however, a Lagrangian analysis of a 3D flow with 2D data can still be suitable, but prior knowledge about the relevant flow structure is needed. Additionally, if the available velocity data are collected at a coarse temporal resolution such that interpolation schemes cannot be used to estimate intermediate velocity fields, the Lagrangian calculations will not be accurate. In Sect. 3 this is shown directly with turbulent channel simulation data, and a potential method of using velocity field evolution models to generate more accurate intermediate velocity fields is shown to alleviate this problem. In the examples presented here, the lack of dimensional support and temporal resolution is shown to significantly affect the FTLE fields, which could result in large-scale misidentification of structures. Much of this can be anticipated or mitigated, however, with a general physical understanding of the flow field of interest.

1.1 Implementing coherent structure analyses

Commonly used Eulerian criteria (vorticity, Q, Δ, λ_{ci}^2, λ_2) evaluate the spatial structure of quantities derived from the instantaneous velocity field and its gradient, and large magnitudes highlight regions of the flow that are highly rotational, e.g. vortex cores (Hunt et al. 1988; Zhou et al. 1999; Chong et al. 1990; Jeong and Hussein 1995). An objective Eulerian criterion, the instantaneous vorticity deviation (IVD), was proposed by Haller et al. (2016) to address some of the shortcomings of previous Eulerian techniques. IVD is defined in Eq. 1 as the magnitude of the vorticity at each location minus the vorticity averaged over the entire spatial domain at that instant in time.

$$IVD(x, t) = |\boldsymbol{\omega}(\boldsymbol{x}, t) - \overline{\omega}(t)| \tag{1}$$

An IVD center is defined as the largest IVD value inside of a vortex. If level sets of IVD are non-increasing in an outward direction from the IVD center, and satisfy a convexity deficiency criterion, the structure is considered an Eulerian vortex. The Eulerian vortex boundary is defined as the outermost IVD level set that satisfies the convexity deficiency criterion. This yields a frame invariant method to determine the locations of vortices and their boundaries in Eulerian data. While this technique removes some of the common problems that many Eulerian criteria share related to frame invariance and thresholding, it is still sensitive to errors in the velocity field due to the use of spatial gradients. A key measure in this manuscript is the out-of-plane IVD core angle, hereafter referred to as the IVD core angle. This is the angle between the fluctuating vorticity (IVD) vector at the IVD core and the plane of interest. A 90° IVD core angle corresponds to a vortex that is perpendicular to the plane, and a 0° IVD core angle corresponds to a vortex that is parallel to the plane.

Lagrangian methods identify coherent structures based on the flow properties along fluid particle trajectories. Many of these methods start with the computation of the idealized particle trajectories through the fluid velocity fields. More precisely, $\boldsymbol{\phi}(t, \boldsymbol{x}_0, t_0)$ denotes the flow map, which contains the positions of all trajectories at time t that began at positions $\boldsymbol{x}_0$ at time t_0. The flow map is defined from a grid of particle trajectories in the flow domain that are advected in time using a fourth-order Runge–Kutta integrator. The coefficient of expansion, σ_τ, is defined in Eq. 2 as the largest eigenvalue of the Cauchy–Green strain tensor, $(\nabla_{\boldsymbol{x}_0}^* \nabla_{\boldsymbol{x}_0})$, where $\nabla_{\boldsymbol{x}_0} = \partial \boldsymbol{\phi}(t_0 + \tau, \boldsymbol{x}_0, t_0)/\partial \boldsymbol{x}_0$, τ is the integration time, and $*$ denotes the matrix transpose operator.

$$\sigma_\tau(\boldsymbol{x}_0, t_0) = \lambda_{\max}(\nabla_{\boldsymbol{x}_0}^* \nabla_{\boldsymbol{x}_0}). \tag{2}$$

One method for identifying Lagrangian coherent structures is the finite-time Lyapunov exponent field (FTLE, Λ), a scalar field defined on the grid from the Cauchy–Green tensor via σ_τ as follows:

$$\Lambda_\tau(\boldsymbol{x}_0, t_0) = \frac{1}{2\tau} \log \sigma_\tau(\boldsymbol{x}_0, t_0). \tag{3}$$

As FTLE is calculated from the largest eigenvalue of the gradient of the flow map, it can be described as a measure of the maximum rate of separation among neighboring particle trajectories initialized near each point. The regions of large magnitude in the FTLE field often depict where there is

separation between qualitatively distinct regions in the flow during the flow map integration, e.g. transport boundaries.

The maximizing ridges of the FTLE field are nearly material lines over the time interval of the particle integration (Shadden et al. 2005). The ridges identified from FTLE calculated by integrating in forward (positive) time are repelling material lines (pFTLE), but FTLE fields can also be computed by integrating flow map trajectories backwards in time. The trajectories that separate in negative (backward) time would converge in positive (forward) time, and, therefore, ridges of the negative FTLE field (nFTLE) indicate local attraction. In this work, only nFTLE fields are calculated as they generally provide more easily identifiable ridges throughout the domain than pFTLE ridges for flows with a significant freestream velocity.

One advantage of using FTLE ridges for analysis in experimental flow fields is their relative insensitivity to short-term anomalies in the velocity field. The method has been shown to be robust and relatively insensitive to imperfect velocity data as long as the errors remain small in a time-weighted norm (Haller 2002). While individual trajectories may be sensitive to velocity field noise or errors, those errors would have to be significantly large and persistent for the resulting trajectories to manifest different nearby topological features. Eulerian criteria often depend on the gradients of the velocity field, making them sensitive to small-scale errors that are common in PIV results. In addition, most Eulerian criteria require a user-defined threshold to indicate the regions where a flow structure exists, which introduces a level of ambiguity in the definition of the structure itself. Thresholding FTLE results, however, narrows the ridges of FTLE, but does not change their location.

More recently, Haller (2011) has exposed some of the vulnerabilities associated with using the ridges of the FTLE fields and showed that not all LCS are FTLE ridges, and that not all FTLE ridges depict hyperbolic LCS in the flow. While the work presented in this paper does not apply the new formalism of that work in identifying hyperbolic LCS, much of the recent work on finding Lagrangian coherent structures starts with a calculation of particle trajectories or the Cauchy–Green strain tensor, if not the FTLE field itself, and, therefore, the observations of this paper remain applicable. In the same way that the lack of dimensional support and temporal resolution significantly reduce the accuracy of the FTLE analysis, it is expected that these factors will affect the variety of methods that extract Lagrangian coherent structures from experimentally obtained fluid dynamic data.

The simulated trajectories used for the 3D and 2D FTLE calculations were initialized only within each 2D plane studied. The 3D FTLE calculation allowed the particles to advect throughout the full 3D domain using all three components of velocity. The 2D FTLE calculation constrained the particles to the plane by setting the out-of-plane component of velocity to zero. The 2D calculation simulated the use of two-dimensional, two-component or three-component velocity data that would be expected from PIV experiments. While stereoscopic PIV is commonly used to extract three-component two-dimensional PIV data, the lack of velocity information in the rest of the domain outside of the PIV plane makes it impossible to track particles during the FTLE integration if the particles leave the data plane. Therefore, the trajectories would still be projected back into the plane in the same manner as they are when the out-of-plane velocity was not known.

A vortex with an IVD core angle lower than 90° will induce velocity out of the data plane. During a 2D nFTLE calculation errors may begin to arise when particles would leave the plane if the out-of-plane velocity information was considered, as in the 3D nFTLE calculation. The particles may no longer experience the same flow physics as they travel through a different portion of the domain and experience different velocities in the 2D and 3D nFTLE calculations. Errors in particle trajectories would be large relative to the "time-weighted norm," and could result in significant errors in the nFTLE ridge locations that could potentially lead to the misrepresentation of the coherent structures in the flow.

2 Data dimension

Two test cases were investigated to identify how FTLE fields are affected when the three-dimensionality of the flow field is not captured. These included an analytical case using Hill's spherical vortex and an experimental case using a full volume reconstruction of the wake behind a trapezoidal pitching panel.

2.1 Hill's spherical vortex

2.1.1 Analytical test case

In order to quantify the degradation of FTLE as a function of the local vortex angle, the simple example of Hill's spherical vortex was used as the first test case. This flow is an analytical solution to Euler's equation that allows for easy calculations of local vortex angles and FTLE boundaries for a single vortex. The velocity field is defined by Hill (1894) and results in a spherical vortex ring with a prescribed radius. For illustrative purposes, a midspan cross section of the streamlines in this axisymmetric spherical vortex ring is shown in Fig. 1a. The velocity components inside and outside of the vortex are as follows:

Fig. 1 Hill's spherical vortex.
a Streamlines in $y/r = 0.0$
plane. **b** Locations of FTLE
planes: green ($y/r = 0.0$), blue
($y/r = 0.32$), and magenta
($y/r = 0.64$)

(a)

(b)
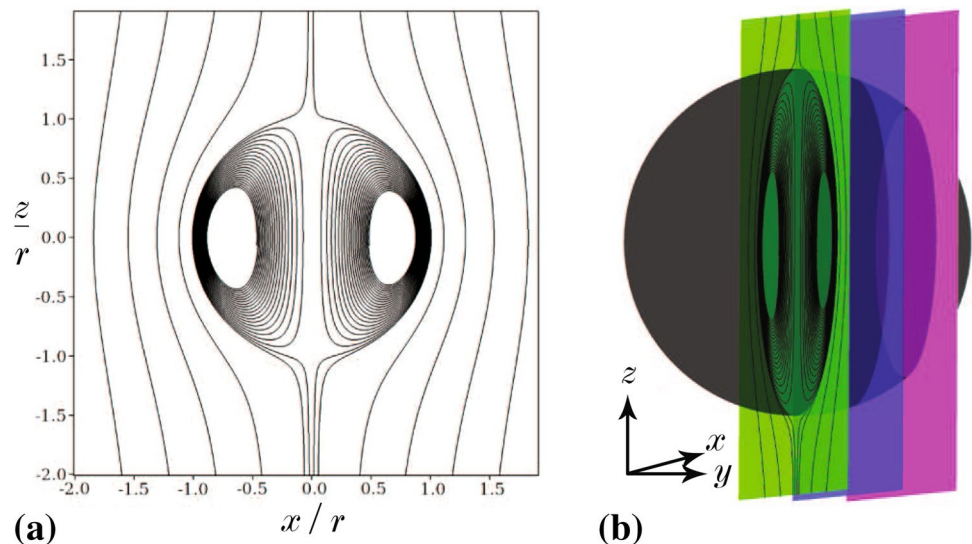
2.1.2 Inside vortex

$$u = \alpha xz/5, \tag{4}$$

$$v = \alpha yz/5, \tag{5}$$

$$w = (\alpha/5)(r^2 - z^2 - 2x^2 - 2y^2), \tag{6}$$

2.1.3 Outside vortex

$$u = \alpha r^5 xz \Big/ \big[5(x^2 + y^2 + z^2)^{(5/2)}\big], \tag{7}$$

$$v = \alpha r^5 yz \Big/ \big[5(x^2 + y^2 + z^2)^{(5/2)}\big], \tag{8}$$

$$w = \frac{-\alpha r^2 \big\{ \big[2(x^2 + y^2 + z^2)^{(5/2)}\big] - 2r^3 z^2 + r^3 y^2 \big\}}{15\big[(x^2 + y^2 + z^2)^{(5/2)}\big]}, \tag{9}$$

where the vortex strength parameter, α, is set as 2, and the vortex radius, r, is unity for this case. While the spherical vortex is 2D (axisymmetric), it provides a systematic change in vortex angle in 3D Cartesian space. Hill's spherical vortex is a ring around the z axis, so y-constant planes are used for this analysis. At $y/r = 0$, two vortex cores can be seen perpendicular to the plane in Fig. 1a. As the plane of computation shifts ($y/r > 0$), the IVD core angle, which is initially at 90°, begins to decrease as the vortices gradually tilt towards their respective y-constant planes. For this case, the IVD core angle is calculated at the location of maximum IVD within each vortex core.

The trajectories used to calculate FTLE were initialized on a 100×100 grid with domain $[x/r] \in [-2.0, 2.0]$ and $[z/r] \in [-2.0, 2.0]$, resulting in a spatial grid spacing of 0.04 in x/r and z/r. An integration time of $1.33t^+$ was

used, where $t^+ = tW_\infty/r$, and W_∞ is the far-field velocity in the z direction. An integration step size of $0.003t^+$ was used in both the 2D and 3D calculations. Since there is only one vortical structure in the flow, a further increase in integration time resulted in thinner FTLE ridges and did not change their location. The out-of-plane velocity (v) was set to zero for the 2D FTLE calculation.

The FTLE ridge overlap percentage, hereafter referred to as the overlap percentage, was calculated by first normalizing the 2D and 3D FTLE fields by their respective global maximum. Then all values below the chosen threshold (55% of the maximum in this case) in the region of interest were set to zero. The number of locations with both 2D and 3D FTLE ridges above the threshold were divided by the number of locations where the 3D ridges were above the threshold. This yields the percentage of the 3D FTLE ridge locations that are also captured by the 2D FTLE ridges. The overlap percentage was chosen over the normalized cross-correlation coefficient because the normalized cross-correlation coefficient is sensitive to small changes in amplitude or area of the ridges, which are not physical changes that affect the identification of vortices.

2.1.4 Analytical results

Figure 1a shows the $y/r = 0$ plane with streamlines highlighting the two cores that are visualized in a planar cut of Hill's spherical vortex, while Fig. 1b shows the locations of the three FTLE planes displayed in Fig. 2.

Slices of 3D and 2D nFTLE ridges are shown in Fig. 2 for planes at $y/r = 0.00$, $y/r = 0.32$, and $y/r = 0.64$. Only FTLE values greater than $0.55\Lambda_{max}$ are plotted, and a black line at the location of the prescribed radius is included. As the normal distance from the $y = 0$ plane increases, the radius of the vortex boundary intersecting the plane of

Fig. 2 3D nFTLE (red) and 2D nFTLE ridges (blue) for Hill's spherical vortex at various y/r values. The prescribed radius is shown in black

(a) $y/r = 0.0$

(b) $y/r = 0.32$

(c) $y/r = 0.64$
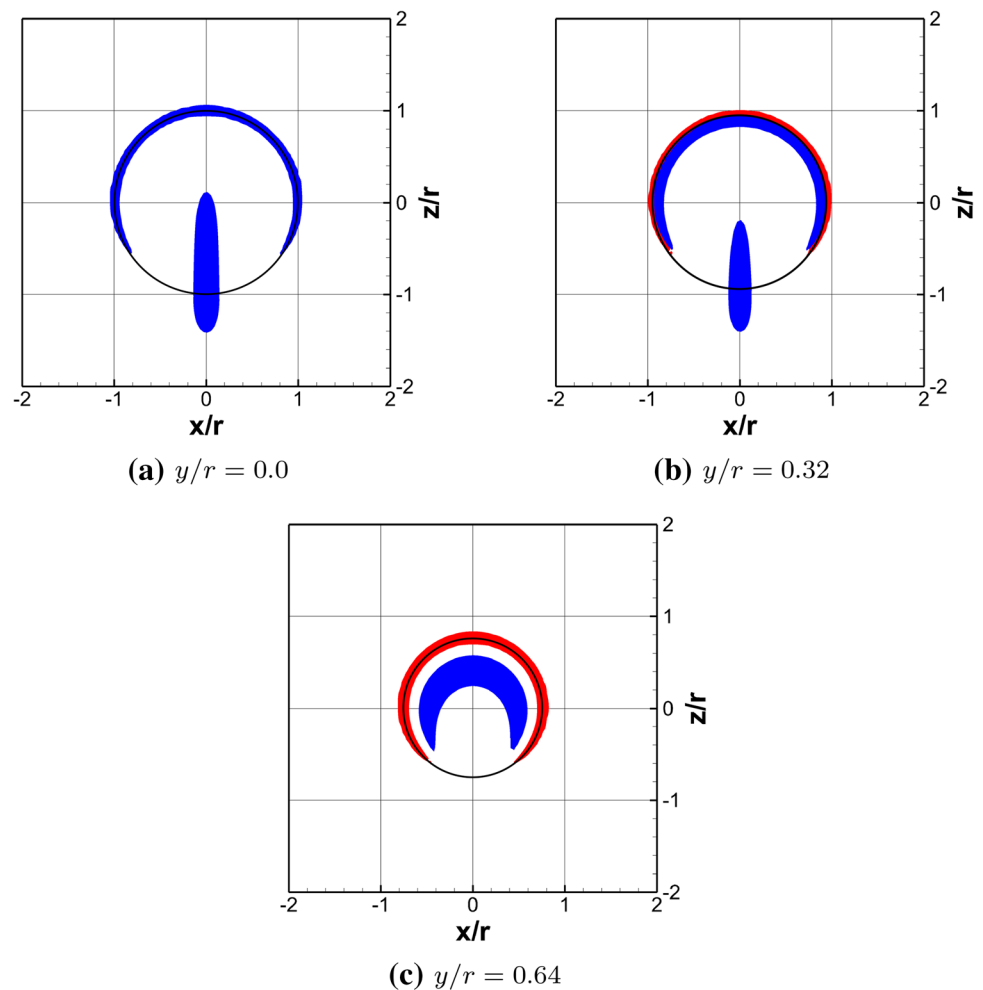
interest decreases, which is consistent with the 3D nFTLE ridges. While this occurs, the local vortex angle decreases, and the 2D FTLE fails to capture the vortex boundary accurately. The ridge of 2D FTLE defining the boundary of the vortex erroneously shifts farther toward the vortex center than the 3D nFTLE ridge does.

Figure 3a displays the overlap percentage values as a function of IVD core angle. The three points that are labeled in the figure (2a, 2b, and 2c) correspond to Fig. 2. When the IVD core is aligned perpendicular to the plane of interest at the midsection of the sphere (90°, Fig. 2a), the 2D FTLE is identical to that of the correct 3D FTLE, as represented by the 100% overlap percentage value. The red 3D FTLE ridges cannot be seen in Fig. 2a as they are obscured by the blue 2D FTLE ridges. As the vortex becomes less perpendicular to the plane, the error in the 2D FTLE increases, resulting in a lower overlap percentage. At $y/r = 0.32$, where the IVD core angle is 70°, the overlap percentage is only 37%. As an alternative to using the overlap percentage to quantify the error, the difference between the 3D and 2D vortex radius as defined by the location of maximum FTLE was extracted

and is presented in Fig. 3b. As the IVD core angle decreases, the error in the radius of the vortex determined by the 2D FTLE increases, as high as 40% in the $y/r = 0.64$ plane. The FTLE errors caused by out-of-plane flow not captured by the 2D FTLE calculation can result in the misidentification of the vortex boundary.

2.2 Experimental wake behind a trapezoidal pitching panel

2.2.1 Experimental test case

A 3D experimental test case was investigated to determine the relationship between lack of dimensional support and FTLE results in a more complex flow field using experimental data. The test case analyzed was the wake behind a trapezoidal pitching panel (Kumar et al. 2016; King et al. 2018; Kumar et al. 2018). The panel approximately models the shape of a fish caudal fin and is made of rigid acrylic. The panel was 1.59 mm thick, had a midspan chord of 101 mm (c), a 52-mm leading edge span, and a 254-mm trailing

(a) Overlap percentage between 2D and 3D nFTLE ridges

(b) Radius percent error difference between 2D FTLE and 3D FTLE
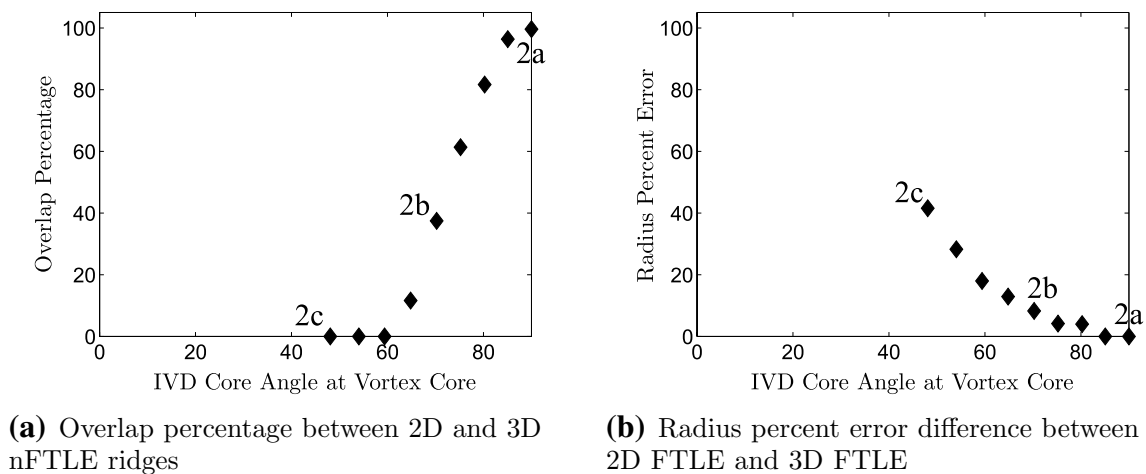
Fig. 3 Error metrics between 2D and 3D FTLE as a function of IVD core angle

edge span. The sweep angle of the panel leading edge was 45°, and the panel was pitched about its leading edge through an angle of $\pm$ 7.5° with 0° inline with the streamwise direction (x). Data at a Strouhal number based on the pitching amplitude of 0.37 and at a Reynolds number based on chord of 7400 were collected using stereoscopic PIV.

Two 1.3 megapixel HiSenseMKI CCD cameras were used to collect three-component velocity data at one plane with a field of view of $[x/c, y/c] = [2.48, 3.07]$. A New Wave Gemini Nd-YAG 200-15 laser was used to illuminate polyamide seeding particles with a diameter of 20μm. 29 spanwise-constant (z = constant) planes of data were taken along the full trailing edge span of the pitching panel using a traverse system. The planes were spaced $\Delta z/c = 0.100$ apart, except near the midpsan, where the spacing was $\Delta z/c = 0.050$, and near the tips of the panel, where the spacing was $\Delta z/c = .020$. Dantec DynamicStudio was used to calculate the vector fields using an interrogation area of 16×16 pixels with a 50% overlap, resulting in a vector field of 120×130 with a spacing of 0.021 in x / c and 0.024 in y / c. The resulting velocity fields were phase-averaged into 24 phases per pitching period, T. The spanwise-constant planes of velocity were interpolated onto a common volumetric grid using a cubic spline. This resulted in a final velocity spacing of $0.020 \times 0.020 \times 0.025$ in x / c, y / c, and z / c, respectively. This resolution was fine enough to allow for accurate calculations of velocity gradients. Representative images of the panel wake at one instant in time visualized by IVD colored by ω_z for two different views are shown in Fig. 4.

A study on the effect of integration time on the nFTLE fields was conducted, and the results for the midspan for the four integration times studied are presented in Fig. 5. The nFTLE fields did not have well-defined ridges throughout the domain until an integration time of 1.5T. Further increases in integration time had a negligible effect on the nFTLE field,

so an integration time of 1.5T was used with an integration step size of 0.005T (or 10 times the temporal resolution of the phase-averaged velocity fields) for both the 2D and 3D calculations. The integration step size was decreased from the step size of the phase-averaged velocity data by linearly interpolating the velocity values at each spatial point for each time between successive velocity fields. This method reduces errors during the particle integration by reducing the step size. It is common for experimentally measured data to have lower temporal resolution than numerical simulations, so an integration step size 5–10 times smaller than the velocity data step size can be used to reduce the error in the particle locations. While this can help reduce errors in the trajectory calculation, significant errors will still occur if the velocity data temporal resolution is not high enough to capture the appropriate length and time scales of the flow, as will be shown in Sect. 3. Generally, 15 to 20 velocity fields per relevant time scale are sufficient to avoid large errors.

Similar to the Hill's vortex case, the overlap percentage of 2D and 3D nFTLE ridges were used as a method to systematically study the relationship between IVD core angles and the corresponding accuracy of 2D FTLE. The IVD core angles for each vortex analyzed in this portion of the study were calculated by averaging the IVD core angle for all points within its outermost IVD level set that satisfied a convexity deficiency of 40%. This value of convexity deficiency means that 40% of the area of the convex hull was not contained within the contour of IVD that was used. The standard deviation distribution of the IVD core angles throughout the domain is roughly Gaussian, with a mean of 13.9°, a minimum of 0°, a maximum of 30.2°, and a standard deviation of 4.1°. A large contributor to the fairly large spread of IVD core angles within a vortex is due to the magnification of any errors in the velocity field by the spatial derivative used to calculate vorticity and IVD. The

Fig. 4 Pitching panel IVD colored by ω_z

(a) Side view   **(b)** Top view

(a) $\tau = 0.5T$ **(b)** $\tau = 1.0T$ **(c)** $\tau = 1.5T$ **(d)** $\tau = 2.0T$
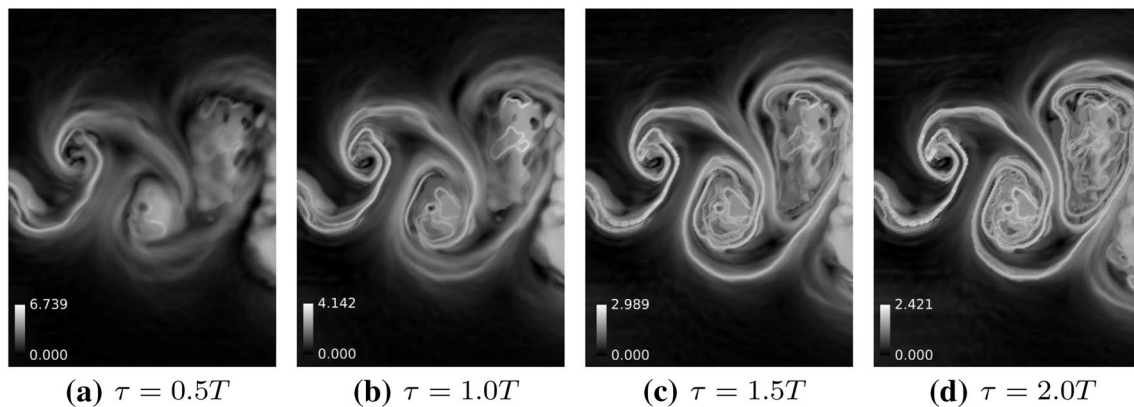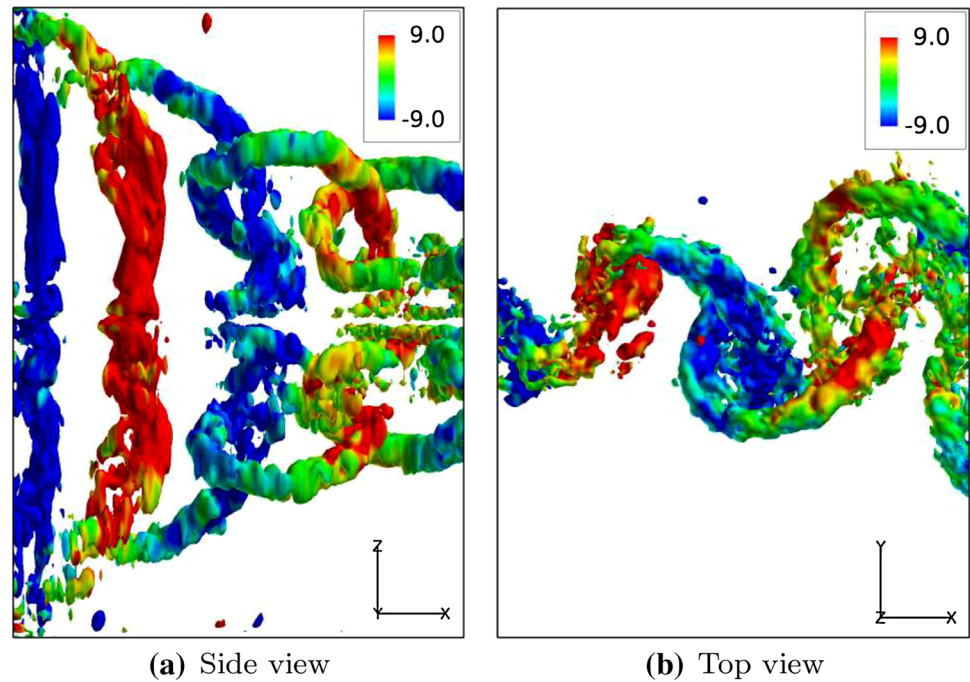
Fig. 5 Variation of 3D nFTLE with integration time in the wake of a trapezoidal pitching panel at the midspan location

FTLE ridge overlap percentage was calculated locally on each spanwise-constant plane in a small region surrounding the portion of the vortex that intersects the plane. An ellipse was fit to the IVD core outer contour, and then the major and minor axes of this ellipse were doubled in size to capture the associated FTLE ridges. A number of ellipse sizes ranging from the IVD outer contour size to tripling the ellipse axes were studied, and the chosen size qualitatively captured the correct FTLE ridges for a majority of the vortices. Areas that were too large captured FTLE ridges associated with neighboring vortices, and areas that were too small did not capture enough of the associated FTLE ridges. Changes in the area considered around each vortex for the overlap percentage calculation did not significantly affect the trend of the results. The relevant area is expected to vary for other

flow fields with different vortex sizes and spacing. FTLE values above $0.55\Lambda_{max}$ were used for the overlap percentage calculation.

2.2.2 Experimental results

Figure 4 shows a representative snapshot of the coherent structures in the wake at one phase in time. The panel periodically sheds spanwise-oriented vortices from its trailing edge as it pitches, and two vortices with oppositely-signed spanwise vorticity are shed each pitching period. The vortices are detected using an isosurface at 28% of the global maximum of IVD and are colored by spanwise vorticity. 3D effects result in the vortices bending near the panel tips, resulting in a wide range of IVD core angle values

throughout the domain. This, coupled with the near constant vortex diameter and relative isolation of each vortex, makes this flow an ideal case for a systematic study.

Comparisons between 3D and 2D nFTLE fields at the panel midspan and quarterspan are shown in Fig. 6. IVD values above 28% of the IVD global maximum are shown in black, which highlight the vortex cores; 3D nFTLE ridges are shown in red, and 2D nFTLE ridges are shown in blue. At the midspan (Fig. 6a) the IVD core angles are 88° and 65° for vortices 1 and 2, respectively. Vortex 1 is aligned almost perfectly perpendicular to the data plane, and the 3D and 2D nFTLE ridges are nearly identical. Vortex 2 is at a lower IVD core angle and there are some discrepancies between the 3D and 2D nFTLE ridges, but the overall shape of the nFTLE ridges surrounding the vortex are similar. At the quarterspan (Fig. 6b) the IVD core angles are 66°, 23°, 48°, and 32° for vortices 3 through 6, respectively. Significant differences are seen between the 3D and 2D nFTLE ridge locations at the quarterspan, especially for angles lower than 60°. The 2D nFTLE ridges for vortices 4 and 5 cut directly through their respective vortices and do not surround them as the 3D nFTLE ridges do. There is only one 2D nFTLE ridge in the vicinity of vortex 6, and it crosses the 3D nFTLE ridges, wholly misrepresenting the vortex location.

The result of a systematic study of nFTLE ridge overlap percentage in the pitching panel wake is shown in Fig. 7. The overlap percentage values are colored by the distance from the trailing edge midspan, normalized by the midspan chord. The IVD core angle was averaged within the inside of each vortex boundary as defined by IVD. The results show a general trend towards higher FTLE ridge overlap percentages with increasing IVD core angle, but the large spread in the data indicates that the relationship is complex. The
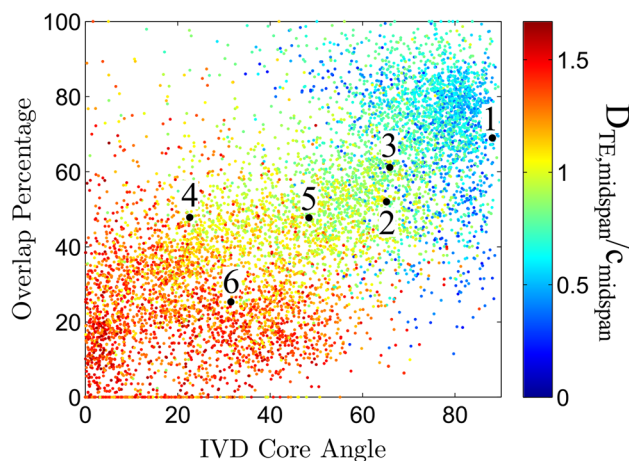

Fig. 7 Overlap percentage compared to IVD core angle colored by distance from the trailing edge midspan normalized by the midspan chord for $\Lambda \geq 0.55\Lambda_{max}$. Black squares and numbers correspond to vortices labeled in Fig. 6

increase in overlap percentage with increasing IVD core angle is roughly linear.

An investigation into the large variation in FTLE overlap percentage values among similar IVD core angles revealed that there is no single metric that captures the reason for the large variation. Some of the spread in the results is likely due to the uncertainty in the IVD core angle determination. Additional metrics investigated include out-of-plane velocity magnitude, out-of-plane shear components, and distance to the nearest vortex. The majority of the points with high overlap percentage values and high IVD core angles are located near the trailing edge midspan (blue points) in regions somewhat isolated from the surrounding vortices. These points

Fig. 6 Pitching panel IVD (black), 3D nFTLE (red), and 2D nFTLE (blue) at two spanwise-constant locations. Vortices are labeled with numbers in black. The IVD core angles for the vortices are the following: $1 = 88°$, $2 = 64°$, $3 = 66°$, $4 = 23°$, $5 = 48°$, and $6 = 32°$

(a) Midspan

(b) Quarterspan
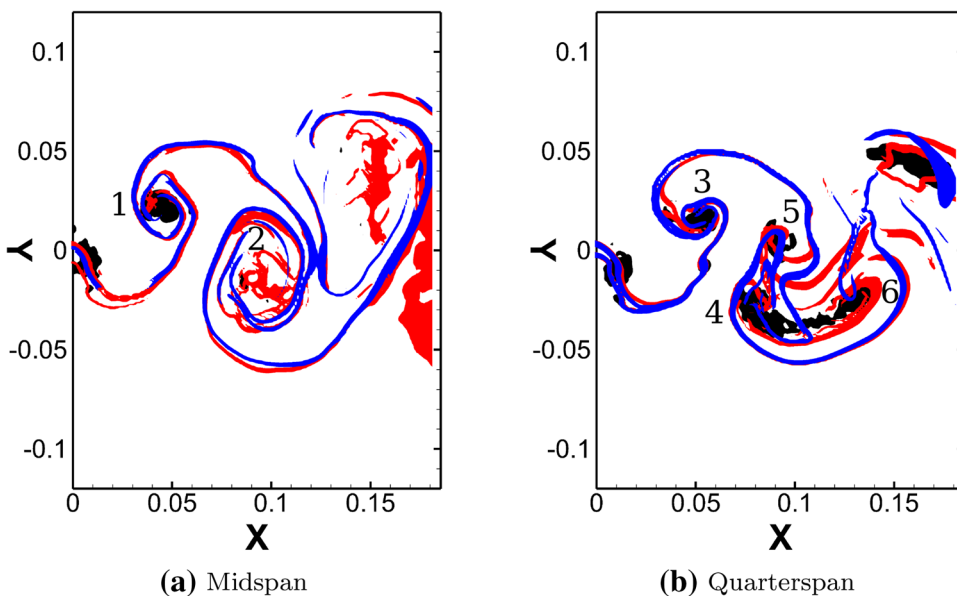
are primarily located in the two vortices closest to the panel trailing edge. Farther downstream, as well as near the tips of the panel, the IVD core angle decreases as the vortices begin bending towards the streamwise and transverse directions. As this happens, the vortices draw closer together and begin to induce large spanwise velocities and spanwise gradients, resulting in low overlap percentage values. The variation in overlap percentages is practically impossible to predict with only planar two-component velocity information. When fluid leaves the plane of interest, it can experience a range of flow physics depending on the specific flow field. Even if three-component velocity data are available, there is no known information on velocity fields outside of the plane of interest that could be used to update the out-of-plane trajectory information. In some cases with nearly 2D flow, the fluid leaving the plane would behave similar to the flow within the plane, resulting in similar FTLE ridge locations. In cases with highly 3D flow fields, complex vortex interactions, or turbulence, the fluid leaving the plane would experience drastically different flow physics, most likely resulting in low overlap percentages.

Figure 8 displays the same results as Fig. 7, but using an FTLE threshold of 0.67 instead of 0.55. Increasing the FTLE threshold value thins the FTLE ridges. The FTLE threshold value used for the overlap percentage affects the exact values for each vortex, but do not change the overall trend.

The angle of the dominant coherent structures can generally be obtained through the application of flow visualization experiments. It should be noted that the exact angle of a specific portion of the coherent structure is not important, but whether the overall alignment of the structure is nearly perpendicular to the plane of interest is the crucial indicator. If the coherent structure is angled significantly
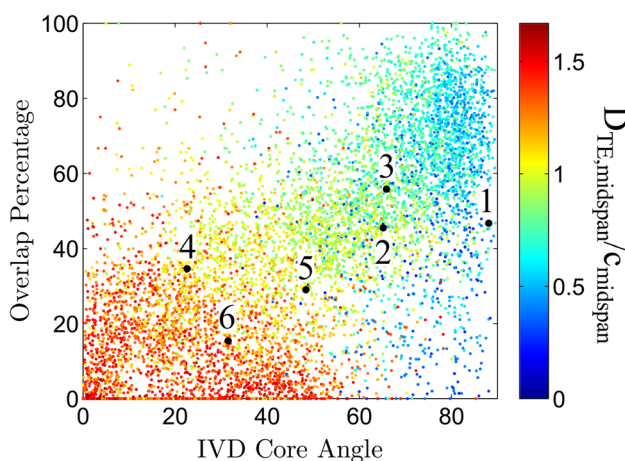
into the plane of interest, or if other vortices are nearby, the FTLE results will likely have large errors as demonstrated by the test cases presented above.
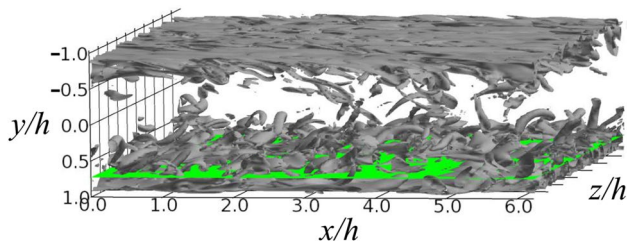
3 Time resolution

In order to implement an effective Lagrangian analysis on discrete data sets, time-resolved velocity data are required in addition to the previously addressed dimensional support, such that interpolation can reasonably be used to recreate velocity fields between data sets. For the numerical integration necessary to compute the flow map, the integration time step is often smaller than the dimensional time between discrete data sets from experimental measurement or numerical simulation.

3.1 Numerical test case

In the following section, data from DNS of a fully turbulent channel are used to demonstrate how nFTLE can be compromised in flows with low temporal resolution. The simulation was run at $Re_\tau = 180$, with $Re_\tau = u_\tau h/\nu$, u_τ being the friction velocity, h being the channel half-height, and ν being the kinematic viscosity. In these quantities, $u_\tau = (\tau_w/\rho)^{1/2}$, where τ_w is the shear stress at the wall and ρ is the density. The computational domain was $x/h = [0, 2\pi]$ in the streamwise direction, $z/h = [0, 2\pi]$ in the spanwise direction, and $y/h = [-1, 1]$ in the wall-normal direction. A grid of $[128 \times 129 \times 128]$ points was used for the velocity, resulting in a resolution of 0.05 in x/h and z/h. The resolution in y/h was variable to resolve the near-wall regions. The domain was bounded by walls at $y/h = 1$ and $y/h = -1$ and had periodic boundary conditions in the streamwise and spanwise directions.

This is the same simulation that was used by Green et al. (2007) and was based on that of Kim et al. (1987). Time was non-dimensionalized as $T^+ = Tu_\tau^2/\nu$, and a non-dimensional trajectory integration time of $T^+ = 27$ was used for the flow map computation. The FTLE field was initialized on a grid with three times higher spatial resolution than the velocity grid in x/h and z/h, and the same resolution as the velocity grid in y/h. This integration time was chosen based on previous results and yields clear, well-defined nFTLE ridges. Little relevant structure is gained by longer integration times, but shorter integration times can result in less sharp nFTLE ridges. A plane located at $y/h = 0.73$ ($y^+ = 49$) was used for the temporal resolution study and is shown in Fig. 9 in green.

Fig. 8 Overlap percentage compared to IVD core angle colored by distance from the trailing edge midspan normalized by the midspan chord for $\Lambda \geq 0.67\Lambda_{max}$. Black dots and numbers correspond to vortices labeled in Fig. 6

Fig. 9 Direct numerical simulation of a fully turbulent channel. Gray isosurface of 8% maximum IVD. Green plane indicates plane of nFTLE calculation at $y/h = 0.73$, $y^+ = 49$

3.2 Numerical results

During the original simulation, data were saved at scaled time increments of $\Delta t^+ = 0.09$. The FTLE calculation was done first using the full time resolution of the data, but additional calculations were done assuming, for example, that only every tenth velocity file was saved ($\Delta t^+ = 0.9$), or that only fiftieth velocity file was saved ($\Delta t^+ = 4.5$). The total

integration time was the same for each case ($T^+ = 27$), as was the integration time step ($\Delta t^+_{\text{int}} = 0.09$). When the integration time step was smaller than the time between velocity fields, both linear and cubic interpolations in time were used to generate intermediate fields for the fixed time step Runge–Kutta 4 integration scheme that was used to calculate the particle trajectories. The results from both interpolation methods yielded similar results, and only those from linear interpolation are shown here for simplicity.

Velocity fields at one instant of time are shown in Fig. 10. Figure 10a shows the streamwise (u) velocity directly output by the DNS. Figure 10b shows the velocity field recreated by linear interpolation between output fields that are separated in time by $\Delta t^+ = 0.9$, and Fig. 10c shows the field recreated by linear interpolations between output fields that are separated in time by $\Delta t^+ = 4.5$. From these images, it can be observed that the recreated velocity field for a data spacing of $\Delta t^+ = 0.9$ is not drastically different from the exact field, but the recreated field for $\Delta t^+ = 4.5$ has changed significantly in the streamwise direction. One can see the same structures in two different positions next to each other

Fig. 10 Streamwise velocity (u) at one instant of time in the turbulent channel, from the DNS output (**a**), and recreated using linear interpolation (**b**, **c**)

(a) $\Delta t^+ = 0.09$

**(b)** $\Delta t^+ = 0.9$

(c) $\Delta t^+ = 4.5$
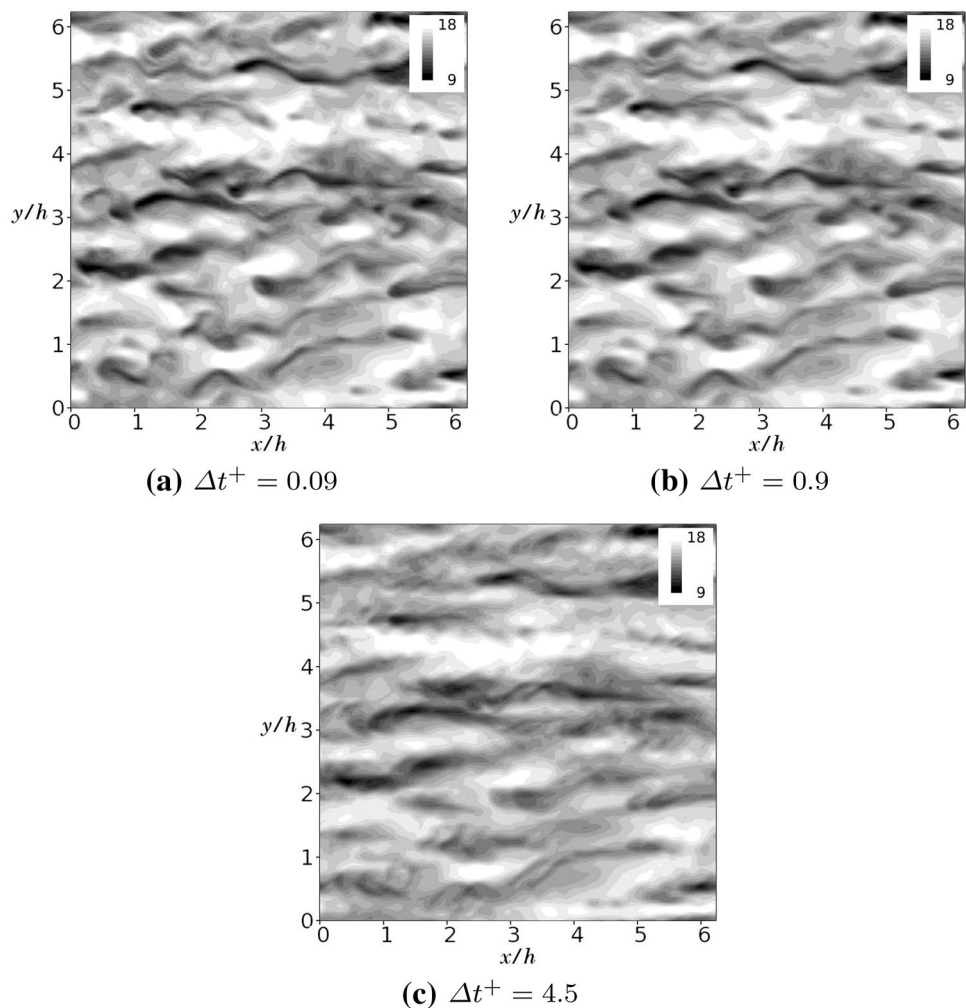
in the streamwise direction, creating a blurred look. This comes from interpolating between two velocity fields that are spaced too far apart in time. From this, it would appear that $\Delta t^+ = 0.9$ may still be a suitable time between data sets, but that the FTLE calculation could start to break down for $\Delta t^+ = 4.5$.

The nFTLE fields calculated using velocity data sets at three different time resolutions are shown in Fig. 11. Both linear and cubic interpolation were used to create the intermediate velocity fields, with no significant differences. As expected from the interpolated velocity fields, for $\Delta t^+ = 0.9$, the general size and shape of nFTLE structures still matched the structures of the nFTLE field calculated using the highest possible time resolution. But when a Δt^+ of 4.5 was

simulated, as in Fig. 11c, there was a drastic, qualitative change in the structure of the FTLE ridges that goes beyond simple spatial filtering. It is clear that the same coherent structure composition is not being captured, although there are regions of similar shape and organization.

Overall, the nFTLE ridges appear to be elongated in the streamwise direction with degrading temporal resolution in a similar manner to the velocity fields shown in Fig. 10, and this effect is gradual as Δt^+ increases. It may, however, be possible to predict this effect since the loss of accuracy in nFTLE is consistent with how the recreated velocity fields degraded for decreasing time resolution of the data. It should also be noted that the higher order interpolation method was not able to mitigate this degradation significantly.
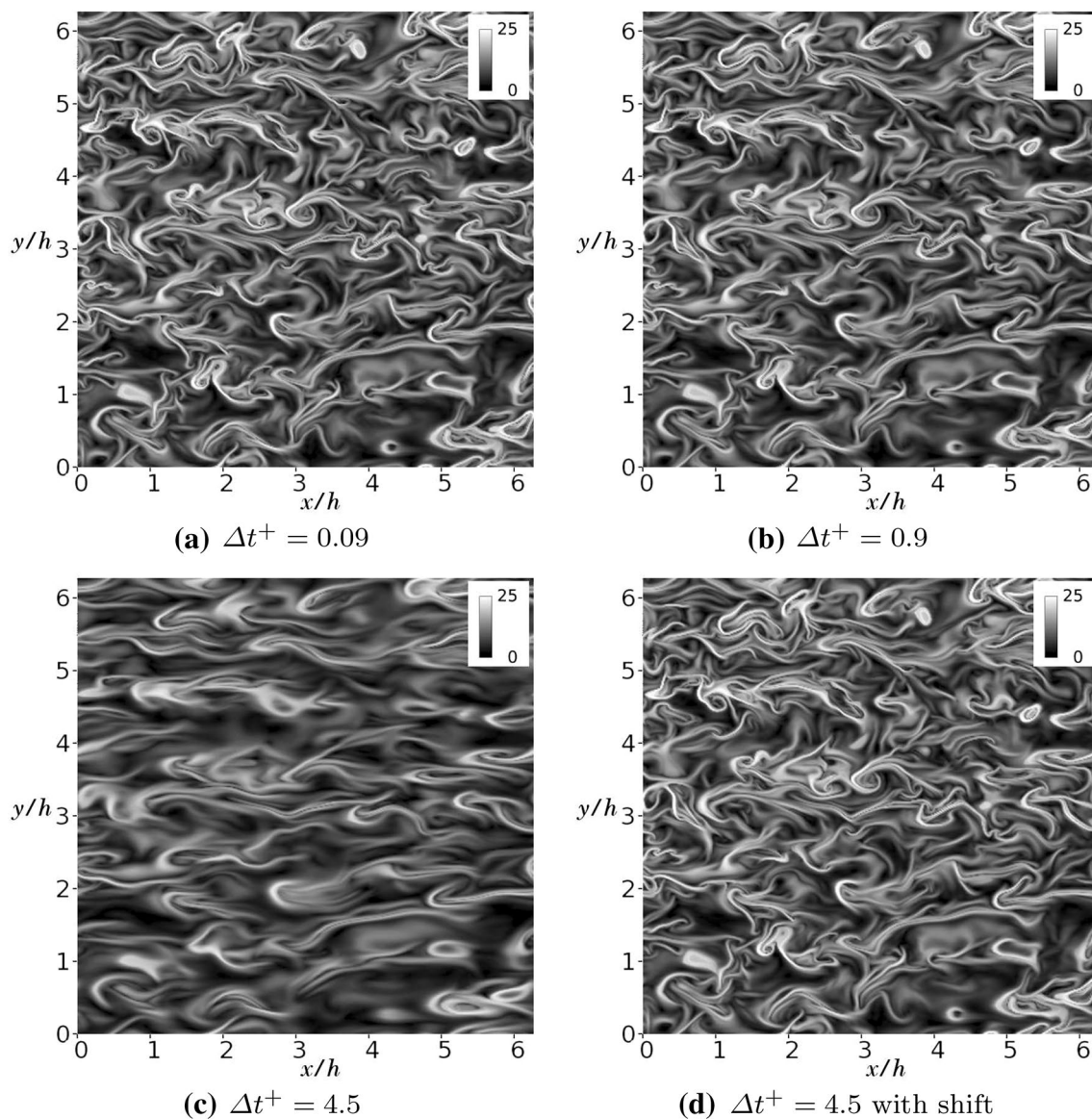
Fig. 11 nFTLE at the same instant of time in the turbulent channel, calculated using full time resolution (**a**), linear interpolation (**b**, **c**) to recreate the intermediate fields, and using velocity field shifting to recreate the intermediate fields (**d**)

In this way, poor temporal resolution can have significant effects on resulting FTLE fields. For an example like the turbulent channel flow, however, there are physical models available for recreating the intermediate velocity fields other than mathematical interpolation schemes. One example is Taylor's frozen eddy hypothesis, which states that the advection contributed by turbulent structures is small compared with the advection of the mean flow (Taylor 1938). This means that the structure of a local region of the velocity field will deform relatively little over a short time span as it is advected with the mean flow.

Here, this concept was used to recreate intermediate velocity fields by shifting a velocity data set along the turbulent channel mean profile ($U(y)$). The mean streamwise velocity profile was obtained by averaging all the available data at each wall-normal location. Consider an estimated 3D velocity field ($\mathbf{u}'$) at a time $t_A + \Delta t$, when t_A is the last time at which velocity data was recorded. The velocity at each point in space is estimated as follows:

$$\mathbf{u}'(x, y, z, t_A + \Delta t) = \mathbf{u}(x - U(y)\Delta t, y, z, t_A). \tag{10}$$

In order to maintain a smooth transition from one velocity field to the next, the intermediate velocity fields were determined by shifting the velocity in each plane according to the mean streamwise velocity at that wall-normal height (y). This was done both forward from the previous data velocity field and backward from the next data velocity field. The two shifted velocity fields were then weighted based on the relative distance in time to their respective data velocity fields and then averaged. This resulted in intermediate velocity fields that smoothly varied from one velocity field to the next, with the intermediate fields determined from a linear weighted average of shifted velocity fields. The turbulent channel nFTLE field that results when using this shifting method for the intermediate velocity is shown in Fig. 11. Here, the coarsest temporal resolution is being used (Δt^+ =4.5), and, therefore, Fig. 11d should be compared with Fig. 11c. While there can still be localized errors between Fig. 11a and d, on the whole, the qualitative structure of the nFTLE field is restored using this well-established model for the velocity field evolution.

While the qualitative structure of nFTLE in the turbulent channel is visibly improved using Taylor's frozen eddy hypothesis instead of large interpolations in time, the quantitative improvement can only be seen with the application of a metric such as the FTLE ridge overlap percentage. The overlap percentage was applied with a threshold of 55% to the temporally resolved FTLE ridges, the FTLE ridges calculated using degraded temporal resolution, and the FTLE ridges calculated from the shifted velocity fields. The resulting overlap percentage values are shown in Fig. 12. As the temporal resolution decreases (Δt^+ increases), the overlap percentage decreases down to about 50% for $\Delta t^+ = 4.5$.
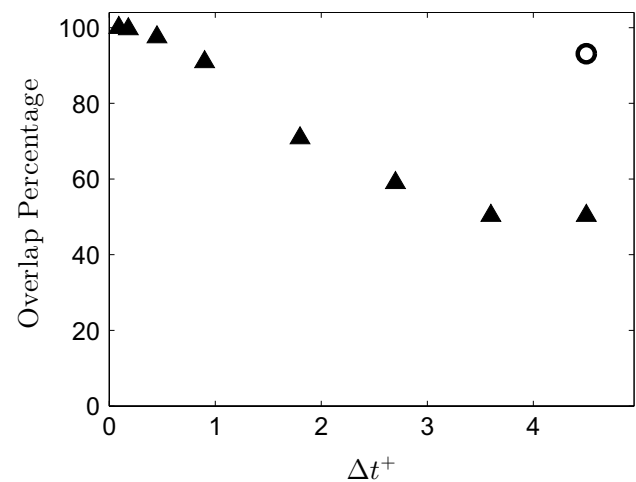
Fig. 12 Overlap percentage values as a function of Δt^+ for calculations using interpolated velocity fields (solid triangles) and shifted velocity fields (hollow circle)

While the shifted velocity fields do not yield a perfect reconstruction of the FTLE, they show a marked improvement of the FTLE ridges, shown by an increase in the FTLE ridge overlap percentage to 93% at the coarsest time resolution.

4 Summary

In order to identify and investigate coherent structures in a range of vortex-dominated fluid flows, from both computational and experimental data, there are a host of tools and methods available. The main characterization is between Eulerian methods, which use the instantaneous velocity field and its gradient to calculate criteria fields which can be scalars or vectors, and Lagrangian methods, which use the quantities calculated along individual particle trajectories to calculate criteria values. The Eulerian criteria are less computationally intensive and give a good indication of the general vortex core location, but the interpretation of the exact location of vortex cores can be subjective, the techniques do not capture structure boundaries accurately, and they are susceptible to noise. The Lagrangian technique employed here, FTLE, which is similar to many other Lagrangian methods used in that it relies on accurate determination of the Cauchy–Green strain tensor from particle trajectory calculations, can yield objective structure boundaries. Often, a comprehensive approach that utilizes both Eulerian and Lagrangian methods can yield the most information.

Despite the clear benefits of including a Lagrangian analysis, there are factors that must be considered before its application. Due to the requirements of accurate particle trajectory integration, temporal resolution and dimensional support are critical. This can be particularly difficult to obtain in

experiments that measure inherently 3D flows, as many velocity measurement techniques are planar. However, if the plane is selected so that the dominant vortices would be aligned normal to the plane, such that the vortex-induced velocities would be contained within the plane, the method may yield sufficient results. To demonstrate this, FTLE fields were calculated in three planes of an analytical test case, Hill's spherical vortex, for two different cases: one in which the full volume of 3D data was used, and a simulated 2D experiment, in which out-of-plane velocities were set to zero in multiple planes across the domain. There were significant differences between the two cases, with the 2D FTLE yielding a decrease in the FTLE ridge overlap percentage as the vortex core angle decreased. This result was followed by a similar comparison between 2D and 3D FTLE for an experimental test case utilizing velocity information in the wake of a trapezoidal pitching panel. The 2D results showed a lack of detail and a change in structure composition when compared with the 3D FTLE.

Last, turbulent channel data were used to demonstrate the importance of data temporal resolution. Simulated experiments of degrading temporal resolution were done by using every tenth velocity data set to calculate FTLE and then by using every fiftieth. The FTLE fields lost detail and structure as the time between data sets increased, even while the integration time step of the Lagrangian particle tracking calculation was held constant. Taylor's hypothesis was used to shift the velocity field along the mean streamwise velocity profile for the times between each velocity data set. This proved to be effective at recovering the original FTLE field, even when using a data time resolution that was fifty times coarser than the original DNS data. While this particular example worked because Taylor's Hypothesis was applicable, it did demonstrate that predictive models that are reliable for at least short times can be very effective at alleviating the negative effects of a poor time resolution.

Previous work has shown the great potential of Lagrangian techniques as a means to investigate applications from both numerical and experimental data. Caution must be taken when applying these techniques to data that may lack dimensional support or temporal resolution, but if those conditions are satisfied, much can be learned analyzing a complete Eulerian and Lagrangian investigation of vortex-dominated flow.

References

Allshouse MR, Peacock T (2015) Refining finite-time Lyapunov exponent ridges and the challenges of classifying them. Chaos Interdiscip J Nonlinear Sci 25(8):087,410

Balasuriya S, Ouellette NT, Rypina II (2018) Generalized Lagrangian coherent structures. Phys D Nonlinear Phenom 372:31–51

Banisch R, Koltai P (2017) Understanding the geometry of transport: diffusion maps for Lagrangian trajectory data unravel coherent sets. Chaos Interdiscip J Nonlinear Sci 27(3):035,804

Beron-Vera F, Olascoaga M, Goni G (2008) Oceanic mesoscale eddies as revealed by Lagrangian coherent structures. Geophys Res Lett 35:L12603

Beron-Vera FJ (2010) Mixing by low- and high-resolution surface geostrophic currents. J Geophys Res Oceans 115(C10):C006006

Blazevski D, Haller G (2014) Hyperbolic and elliptic transport barriers in three-dimensional unsteady flows. Phys D Nonlinear Phenom 273:46–62

Bose C, Sarkar S (2018) Investigating chaotic wake dynamics past a flapping airfoil and the role of vortex interactions behind the chaotic transition. Phys Fluids 30(4):047,101

Bourgeois J, Sattari P, Martinuzzi R (2012) Coherent vortical and straining structures in the finite wall-mounted square cylinder wake. Int J Heat Fluid Flow 35:130–140 **[7th symposium on turbulence and shear flow phenomena (TSFP7)]**

BozorgMagham AE, Ross SD (2015) Atmospheric Lagrangian coherent structures considering unresolved turbulence and forecast uncertainty. Commun Nonlinear Sci Numer Simul 22(1):964–979

Chong MS, Perry AE, Cantwell BJ (1990) A general classification of three-dimensional flow fields. Phys Fluids A 2(5):765–777

du Toit P, Marsden J (2010) Horseshoes in hurricanes. J Fixed Point Theory Appl 7:351–384. https://doi.org/10.1007/s11784-010-0028-6

Froyland G, Padberg-Gehle K (2015) A rough-and-ready cluster-based approach for extracting finite-time coherent sets from sparse and incomplete trajectory data. Chaos 25(8):087406

Froyland G, Santitissadeekorn N, Monahan A (2010) Transport in time-dependent dynamical systems: finite-time coherent sets. Chaos Interdiscip J Nonlinear Sci 20(4):043116

Green MA, Rowley CW, Haller G (2007) Detection of Lagrangian coherent structures in three-dimensional turbulence. J Fluid Mech 572:111–120

Green MA, Rowley CW, Smits AJ (2011) The unsteady three-dimensional wake produced by a trapezoidal pitching panel. J Fluid Mech 685:117–145

Haller G (2002) Lagrangian coherent structures from approximate velocity data. Phys Fluids 14(6):1851–1861

Haller G (2011) A variational theory of hyperbolic Lagrangian coherent structures. Phys D Nonlinear Phenom 240(7):574–598

Haller G (2015) Lagrangian coherent structures. Annu Rev Fluid Mech 47:137–162

Haller G, Hadjighasem A, Farazmand M, Huhn F (2016) Defining coherent vortices objectively from the vorticity. J Fluid Mech 795:136–173

Hernández-Carrasco I, López C, Hernández-García E, Turiel A (2011) How reliable are finite-size Lyapunov exponents for the assessment of ocean dynamics? Ocean Model 36(3–4):208–218

Hill MJM (1894) On a spherical vortex. Philos Trans R Soc Lond (A) 185:213–245

Hunt JCR, Wray AA, Moin P (1988) Eddies, stream, and convergence zones in turbulent flows. Center for Turbulence Research Report CTR-S88

Jeong J, Hussein F (1995) On the identification of a vortex. J Fluid Mech 285:69–94

Karrasch D, Haller G (2013) Do finite-size Lyapunov exponents detect coherent structures? Chaos Interdiscip J Nonlinear Sci 23(4):043,126

Keating SR, Smith KS, Kramer PR (2011) Diagnosing lateral mixing in the upper ocean with virtual tracers: Spatial and temporal resolution dependence. J Phys Oceanogr 41(8):1512–1534

Kim J, Moin P, Moser R (1987) Turbulence statistics in fully developed channel flow at low Reynolds number. J Fluid Mech 177:133–166

King JT, Kumar R, Green MA (2018) Experimental observations of the three-dimensional wake structures and dynamics generated by a rigid, bioinspired pitching panel. Phys Rev Fluids 3(3):034,701

Kourentis L, Konstantinidis E (2011) Uncovering large-scale coherent structures in natural and forced turbulent wakes by combining PIV, POD, and FTLE. Exp Fluids 52(3):749–763

Kumar R, King JT, Green MA (2016) Momentum distribution in the wake of a trapezoidal pitching panel. Mar Technol Soc J 50(5):9–23

Kumar R, King JT, Green MA (2018) Three-dimensional pitching panel wake: Lagrangian analysis and momentum distribution from experiments. AIAA J. https://doi.org/10.2514/1.J056621

Leung S (2011) An Eulerian approach for computing the finite time Lyapunov exponent. J Comput Phys 230(9):3500–3524

Leung S (2013) The backward phase flow method for the Eulerian finite time Lyapunov exponent computations. Chaos Interdiscip J Nonlinear Sci 23(4):043,132

Miron P, Vétel J (2015) Towards the detection of moving separation in unsteady flows. J Fluid Mech 779:819–841

Mulleners K, Raffel M (2011) The onset of dynamic stall revisited. Exp Fluids 52(3):779–793

O'Farrell C, Dabiri JO (2014) Pinch-off of non-axisymmetric vortex rings. J Fluid Mech 740:61–96

Olcay AB, Pottebaum TS, Krueger PS (2010) Sensitivity of Lagrangian coherent structure identification to flow field resolution and random errors. Chaos Interdiscip J Nonlinear Sci 20(1):017506

Poje AC, Haza AC, Özgökmen TM, Magaldi MG, Garraffo ZD (2010) Resolution dependent relative dispersion statistics in a hierarchy of ocean models. Ocean Model 31(1–2):36–50

Rempel EL, Chian ACL, Brandenburg A, Muñoz PR, Shadden SC (2013) Coherent structures and the saturation of a nonlinear dynamo. J Fluid Mech 729:309–329

Rockwood MP, Taira K, Green MA (2016) Detecting vortex formation and shedding in cylinder wakes using Lagrangian coherent structures. AIAA J 55:15–23

Shadden S, Lekien F, Marsden J (2005) Definition and properties of Lagrangian coherent structures from finite-time Lyapunov exponents in two-dimensional aperiodic flows. Phys D 212:271–304

Sulman MHM, Huntley HS, Lipphardt BL Jr, Kirwan AD Jr (2013) Leaving flatland: diagnostics for Lagrangian coherent structures in three-dimensional flows. Phys D Nonlinear Phenom 258:77–92

Tang W, Walker P (2012) Finite-time statistics of scalar diffusion in Lagrangian coherent structures. Phys Rev E 86(4):045,201

Taylor GI (1938) The spectrum of turbulence. Proc R Soc Lond Ser A Math Phys Sci 164(919):476–490

You G, Leung S (2018) An improved Eulerian approach for the finite time Lyapunov exponent. J Sci Comput 76(3):1407–1435

Zhou J, Adrian RJ, Balachandar S, Kendall TM (1999) Mechanisms for generating coherent packets of hairpin vortices in channel flow. J Fluid Mech 387:353–396